Efficient $^1O_2$ production from H_2O_2 over lattice distortion controlled spinel ferrites

Yilan Jiang [a], Peifang Wang [a,*], Tingyue Chen [a], Keyi Gao [a], Yiran Xiong [a], Yin Lu [a], Dionysios D. Dionysiou [b], Dawei Wang [a,*]

[a] *Key Laboratory of Integrated Regulation and Resource Development on Shallow Lake of Ministry of Education, College of Environment, Hohai University, Nanjing 210098, PR China*
[b] *Environmental Engineering and Science Program, Department of Chemical and Environmental Engineering, University of Cincinnati, Cincinnati, OH 45221, USA*

ARTICLE INFO

ABSTRACT

Iron-based materials are difficult to produce single oxygen ($^1O_2$) efficiently from H_2O_2. Herein, we demonstrate that $^1O_2$ production from H_2O_2 can be manipulated by regulating the lattice distortion degrees of spinel ferrite through controlling the contents of Co and Ni in $Co_{1-x}Ni_xFe_2O_4$. Typically, $NiFe_2O_4$, which owns the lowest lattice distortion degree, can produce $^1O_2$ as the dominated reactive oxygen species with $\cdot O_2^-$ as the intermediate. Due to the production of $^1O_2$, the $NiFe_2O_4/H_2O_2$ system removes bisphenol A (BPA) completely within 180 min but removes only $\sim 4\%$ of benzoic acid. In addition, the system demonstrates significant resistance to water matrix interference, as 50 mM of Cl^-, NO_3^-, $H_2PO_4^-$, and humic acid inhibited the BPA degradation by only $\sim0\%$, $\sim2\%$, $\sim40\%$, and $\sim3\%$, respectively. Our work may shed light for regulating the formation of $^1O_2$ from H_2O_2 through the rational design of iron-based catalysts for Fenton-like reactions.

1. Introduction

Fenton and Fenton-like reactions have been widely explored in a variety of applications, including biological sensing, chemical synthesis, and environmental remediation, *etc.*, as they can produce several reactive oxygen species (ROS) [1,2]. As the primary ROS generated during the reactions, $\cdot OH$ can be produced from the Haber–Weiss cycle or high-valent iron-oxo species [Fe(IV)=O/Fe(V)=O] formed via the Bray–Gorin pathway [3–5]. In addition to $\cdot OH$, some other secondary ROS, such as $\cdot O_2^-$ and $^1O_2$, can be formed as well, making the Fenton-like system complicated [6,7]. In the field of water treatment, these formation pathways of ROS have been of great research interest. Specifically, $\cdot OH$ with strong oxidation capacity ($E_0 = 2.8$ V) is non-selective, and its performance regarding oxidation of organic compounds can be hindered in the presence of other constituents in a complex water matrix [8], while $^1O_2$ with lower redox potential ($E_0 = 2.2$ V) reacts with target pollutants exhibit less interferences by other constituents in the water matrix, such as Cl^-, NO_3^-, humic acid (HA), *etc.* [9–11]. As a result, accelerating the efficiency of Fenton-like reactions through the manipulation of $^1O_2$ generation pathway is significant.

Very few strategies have been proposed to manipulate the

production pathway of $^1O_2$ during Fenton-like reactions. For example, Yang et al. proposed that by anchoring Fe_2O_3 nanoparticles within carbon nanotubes to create a nanoconfined zone, $^1O_2$ can be selectively produced as major ROS, instead of $\cdot OH$ [12]. Yi et al. reported that the addition of molybdenum cocatalyst in Fenton system can trigger $^1O_2$ production by improving the Fe^{3+}/Fe^{2+} cycling efficiency and weakening the production of $\cdot OH$ [13]. While these two different strategies open new doors for the manipulation of ROS generation pathways during Fenton-like reactions, no efforts have been made through rational design of iron-based catalysts themselves, which has been believed to be mediated by $\cdot OH$ or high-valent iron-oxo species [3–5]. Since numerous iron-based materials have been considered as efficient catalysts for Fenton-like reactions [14,15], it is of practical importance to develop a strategy to manipulate the $^1O_2$ production during Fenton-like reactions by regulating the structure-dependent properties of iron-based catalysts.

In fact, this structure regulation strategy has been demonstrated regarding the activation of peroxymonosulfate (PMS) or peroxydisulfate (PDS). It has been proven that by regulating the components and coordination of $Co-N-C$ catalysts and coordination atoms in N-doped carbon supported single-atom catalysts, $^1O_2$ generation from the activated

---

PMS can be enhanced [16,17]. Inspired by these efforts, we hypothesized that by rationally regulating the structure and composition of iron-based catalysts, manipulation of ROS generation pathways and high $^1O_2$ production rate can also be achieved in the Fenton-like reactions.

To test our hypothesis, we chose a transition metal spinel ferrite as a model catalyst ($CoFe_2O_4$), since transition metal ferrites are generally considered as efficient catalysts for Fenton-like reactions [18]. As a type of bimetallic oxide, $CoFe_2O_4$ owns an inverse spinel structure, in which O forms the face centered cubic (fcc) packing with Co^{2+}. Co^{2+} occupies the octahedral (Oh) interstitial site and Fe^{3+} distributes uniformly onto the Oh and tetrahedral (Td) sites [19]. Due to the electron transfer between different valence states of the Oh site metal, this structure can provide sufficient surface sites for the adsorption and activation of H_2O_2 [20,21]. More importantly, the high structural tolerance indicates that $CoFe_2O_4$ can accommodate guest metal ions [22]. When different amounts of Ni were introduced to replace Co at Oh sites of $CoFe_2O_4$, $Co_{1-x}Ni_xFe_2O_4$ with varying lattice distortion degree were produced. With bisphenol A (BPA) as a model pollutant and $Co_{1-x}Ni_xFe_2O_4$ as the catalyst, a lattice structure-dependent degradation performance was observed in the Fenton-like reactions. Specifically, when Co was fully replaced by Ni, the lattice distortion degree decreased but the proportion of $^1O_2$ among the generated ROS increased, which improved the selectivity of the Fenton-like system towards BPA degradation.

2. Experimental section

2.1. Materials

Ferric nitrate nonahydrate ($Fe(NO_3)_3·9 H_2O$, > 98.5%), nickel nitrate hexahydrate ($Ni(NO_3)_2·6 H_2O$, 99%), cobalt nitrate hexahydrate ($Co(NO_3)_2·6 H_2O$, 98.5%), sodium hydroxide (NaOH, 96%), hydrogen peroxide (H_2O_2, 30%), sodium sulfite (Na_2SO_3, 97%), potassium chloride (KCl, 99.5%), potassium nitrate (KNO_3, 99%), potassium dihydrogen phosphate (KH_2PO_4, 99%), isopropyl alcohol (IPA, 99.7%), phosphoric acid (H_3PO_4, 85%), and ferrous sulfate heptahydrate ($FeSO_4·7 H_2O$, > 98.5%) were purchased from Sinopharm Chemical Reagent Co., Ltd.; BPA (99%) was purchased from Shanghai Yuanye Bio-Technology Co., Ltd.; HA (90%), furfuryl alcohol (FFA, 97%), nano zero valent iron (nZVI, 99.9%) and benzoic acid (BA, 99.5%) were purchased from Shanghai Aladdin Biochemical Technology Co., Ltd.; p-benzoquinone (p-BQ, 99%) and L-histidine (L-his, chromatographic purity) was purchased from Shanghai Huixing Biochemical Technology Co., Ltd.; Methanol (≥99.9%) was purchased from Merck KGaA. Hydrochloric acid (HCl, 36–38%) was purchased from Shanghai Lingfeng Chemical Reagent Co., Ltd. And 5,5-dimethyl-1-pyrroline N-oxide (DMPO) were purchased from DOJINDO Laboratories. 2,2,6,6-tetramethyl-4-piperidinol (TEMP) was purchased from Nanjing Lisheng Kanghe Biotechnology Co., Ltd. All the chemicals were used without further purification.

2.2. The preparation and characterization methods of catalyst

$Co_{1-x}Ni_xFe_2O_4$ (x = 0, 0.25, 0.5, 0.75, 1) catalysts were prepared by a hydrothermal method. Firstly, $Co(NO_3)_3·6 H_2O$, $Fe(NO_3)_3·9 H_2O$ and $Ni(NO_3)_3·6 H_2O$ with a certain stoichiometric ratio were dissolved in 20 mL deionized water under magnetic stirring. Then, 20 mL of 2 M KOH was added. After stirring for 1 h, the homogeneous solution was transferred into a 100 mL sealed Teflon-lined autoclave and kept at 160 °C for 10 h. The precipitate was washed with distilled water and centrifuged several times. Eventually, the sample was dried at 60 °C for 12 h. Detailed dosing amounts of precursors for different $Co_{1-x}Ni_xFe_2O_4$ catalysts are listed in the supplementary information (Table S1). The characterization methods of catalysts are detailed in Text S1. The previous steps were the same for the preparation of NiO and Fe_2O_3, which only adding $Fe(NO_3)_3·9 H_2O$ or $Ni(NO_3)_3·6 H_2O$, and after dried, the obtained powder were heated at 400 °C for 2 h.

2.3. Determination of degradation process

The degradation experiments were carried out in 100 mL beaker with 50 mL of BPA solution (0.1 mM). pH ranging from 3.0 to 9.0 was adjusted with HCl (2 M) and NaOH (2 M), H_2O_2 concentration was in the range of 0–30 mM and $Co_{1-x}Ni_xFe_2O_4$ concentration was 2.0 g/L. In a typical experiment, the $Co_{1-x}Ni_xFe_2O_4$ was added into the BPA solution and the pH was adjusted, under stirring for 30 min to reach adsorption equilibrium. Afterward, a certain amount of H_2O_2 was quickly spiked to initiate the reaction. Aliquots of the solution was sampled at set time interval. To quench the possible reactions from excessing amount of H_2O_2, 20 μL of 2 M Na_2SO_3 solution was immediately spiked into the samples, which was subsequently filtered with a 0.22 μm Teflon (PTFE) membrane filter and analyzed immediately with HPLC instrument (details of the conditions of the HPLC analysis are provided further below). The removal ratio of BPA was calculated by C/C_0, where C was the concentration of BPA at given time and C_0 was the initial concentration of BPA.

To test the interfering effects of water components, KCl, KNO_3, KH_2PO_4 (5 mM or 50 mM) or HA (50 mg/L or 100 mg/L) was added into the BPA solution, while other experimental parameters remained the same. pH was adjusted to 3.0 for these experiments. For comparison, the influence of interfering ions on the conventional Fenton reaction was also explored. $FeSO_4·7 H_2O$ was used as the source of Fe^{2+}. The reaction conditions for the Fe^{2+}/H_2O_2 system was $c(Fe^{2+})$= 0.02 mM, $c(H_2O_2)$= 4 mM, pH= 3.0. Under such condition, this system showed a similar removal ratio of BPA as the $NiFe_2O_4/H_2O_2$ system did. For the BA degradation experiment, the concentration of BA was 0.1 mM, the catalyst loading was 2 g/L, the pH was adjusted to 3.0, and the concentration of H_2O_2 was 20 mM.

The concentrations of BPA and BA were measured by a high-performance liquid chromatography (HPLC) instrument. For BPA measurement, methanol/deionized water (70:30 v/v) was used as the mobile phase and the wavelength was set at 280 nm. For BA measurement, methanol/water (1 mM H_3PO_4) (50:50 v/v) was used as the mobile phase and the wavelength was set at 227 nm. The injection volume was 20 μL and flow rate of mobile phase was 1 mL/min. The detection limit of BPA and BA was 0.05 mg/L and 0.1 mg/L, respectively.

The rate constant of the catalytic reactions followed the pseudo-first-order model as follows (Eq. 1):

$$\ln \frac{C}{C_0} = -kt \qquad (1)$$

where C (mg L^{-1}) is the target pollutant concentration, t (min) is the reaction time, and k (min^{-1}) is the pseudo-first-order rate constant.

2.4. Identification and quantitative estimation of ROS

Scavenging experiments of ROS were performed as follows : A certain amount of $Co_{1-x}Ni_xFe_2O_4$ was added into the 0.1 mM BPA solution. Subsequently, scavengers of 100 mM IPA ($k_{IPA·OH}$= 6×10^9 M^{-1} s^{-1}), 10 mM p-BQ ($k_{p-BQ·O2}$= 6×10^9 M^{-1} s^{-1}) and 10 mM L-his ($k_{L-his·1O2}$= 3.2×10^7) were separately added into the solution to probe ·OH, ·O_2^- and $^1O_2$, respectively [23–25]. Then, the solution pH was adjusted to 3.0 using 2 M HCl. The subsequent steps were consistent with those experiments without any scavengers. The contribution rate of each ROS (RC) was estimated by the following Eqs. [26]:

$$RC·OH = \frac{k_{·OH}}{k_{app}} \approx \frac{k_{app} - k_{IPA}}{k_{app}} \qquad (2)$$

$$RC·O_2^- = \frac{k_{·o_2^-}}{k_{app}} \approx \frac{k_{app} - k_p - BQ}{k_{app}} \qquad (3)$$

$$RC^1O_2 = \frac{k_{1o_2}}{k_{app}} \approx \frac{k_{app} - k_{L-his}}{k_{app}} \qquad (4)$$
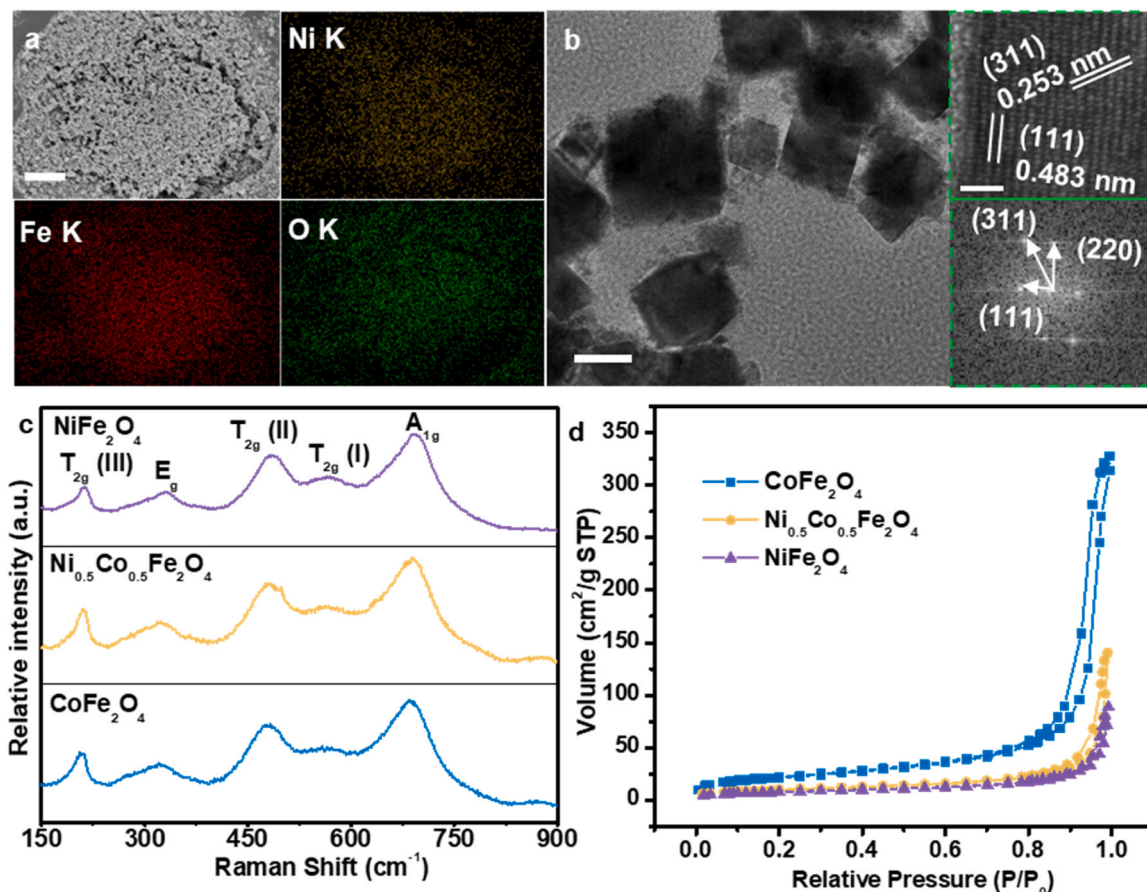
Fig. 1. (a) SEM and EDX mapping images of NiFe₂O₄; scale bars represent 2 μm; (b) TEM, HRTEM images and FFT pattern of NiFe₂O₄; scale bars in TEM and HRTEM images represent 50 nm and 2 nm, respectively; (c) Raman scattering spectra and (d) surface area (SA) analysis of CoFe₂O₄, Ni₀.₅Co₀.₅Fe₂O₄, and NiFe₂O₄.

where RC, k_{app}, k_{IPA}, $k_{p\text{-}BQ}$ and $k_{L\text{-}his}$ represent the radical contribution percentage and the apparent rate constant for BPA degradation in the absence and in the presence of IPA, p-BQ and L-his, respectively.

Electron paramagnetic resonance (EPR) was used to further confirm ROS by reacting with DMPO and TEMP. The pH of DMPO and TEMP solution were both adjusted to 3.0 prior to use. 1 mL of sample was collected from the NiFe₂O₄/H₂O₂ reaction system (catalyst: 2 g/L, H₂O₂: 50 mM and pH: 3.0), then 100 μL of DMPO or TEMP solution were mixed with the samples before the measurement of spin-trapping adducts in the EPR instrument. To explore the source of ¹O₂, 0.1 M of IPA or 0.01 M p-BQ solution was added as scavenging agents for·OH and·O₂ in the solution with TEMP. Spin-trapping adducts are measured before and after H₂O₂ addition under the pH was 3.0.

In addition, 0.1 mM FFA was employed as molecular probe to measure the amount of ¹O₂ produced during the Fenton-like reaction. FFA concentrations were measured using HPLC: methanol/H₂O (50:50 v/v) was used as the mobile phase, and the detection wavelength was set at 219 nm. The steady-state concentration of ¹O₂ ([¹O₂]$_{SS}$) was determined by the loss of FFA, which reacts with ¹O₂ at a second-order reaction rate constant of $k_{FFA,1O2} = 1.2 \times 10^8$ M⁻¹ s⁻¹, using the Eqs. 5, 6 [27–29].

$$FFA + {}^1O_2 \rightarrow Intermediates \tag{5}$$

$$-d[FFA]/dt = k_{FFA,1O2}\,[{}^1O_2]_{SS}\,[FFA] = k_{obs}\,[FFA] \tag{6}$$

where [FFA] is the concentration of FFA (mol L⁻¹); [¹O₂]$_{SS}$ is the steady-state concentration of ¹O₂ (mol L⁻¹); $k_{FFA,1O2}$ is the second-order reaction rate constant for the reaction of FFA with ¹O₂ (M⁻¹ s⁻¹); and k_{obs} is the degradation rate of FFA (s⁻¹).

In spite of being the most efficient scavenger, FFA was able to

intercept only 55% of the ¹O₂ generated [30]. As a result, the cumulative ¹O₂ can be estimated as Eq. 7,

$$cumulative\ {}^1O_2\ produced = ([FFA]_0\text{-}[FFA])/0.55 \tag{7}$$

To quantify the production of·OH, a probe reaction was conducted by oxidizing BA to p-hydroxybenzoic acid (p-HBA). The concentration of BA was chosen as 10 mM, and the initial pH value of the solution was 3.0. The p-HBA was quantitatively analyzed using the HPLC and the mobile phase was a mixture of acetonitrile and 0.1% H₃PO₄ aqueous solution (35:65, v/v) at a flow rate of 1 mL/min, with the detection wavelength at 255 nm [31–33].

$$cumulative\ OH\bullet\ produced = [p\text{-}HBA] \times 5.87 \tag{8}$$

where [p-HBA] is the concentration of p-HBA (mol L⁻¹).

Details on electrochemical measurements and the density functional theory (DFT) calculations were illustrated in the supporting information.

3. Results and Discussion

3.1. Characterization and catalytic performance of $Co_{1-x}Ni_xFe_2O_4$

The X-ray diffraction (XRD) patterns of Ni$_x$Co$_{1-x}$Fe₂O₄ are shown in Fig. S1. All ferrites presented the typical diffraction peaks of cubic symmetry with the Fd-3 m space group, which are consistent with the standard pattern of NiFe₂O₄ (JCPDS no. 74–2081) and CoFe₂O₄ (JCPDS no. 22–1086). No extra diffraction peaks were observed, suggesting that the prepared iron-based catalysts are of high structural purity. The original CoFe₂O₄ showed an irregular shape according to the scanning
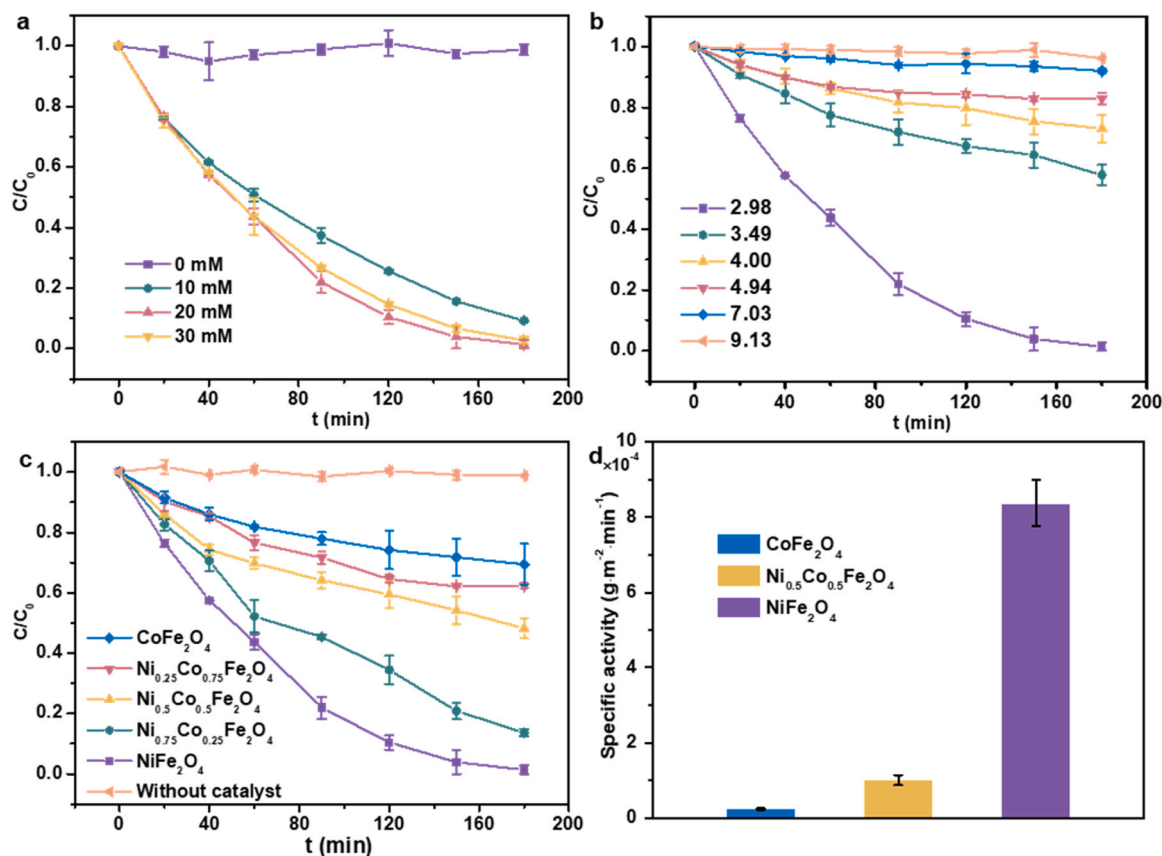
Fig. 2. Different influencing factors of NiFe$_2$O$_4$ catalytic Fenton reaction for the degradation of 0.1 mM BPA. (a) H$_2$O$_2$ concentrations (pH = 3.0); (b) pH values (20 mM H$_2$O$_2$); (c) Degradation kinetics of BPA by Co$_{1-x}$Ni$_x$Fe$_2$O$_4$/H$_2$O$_2$ system; (d) SA-normalized k of CoFe$_2$O$_4$, Ni$_{0.5}$Co$_{0.5}$Fe$_2$O$_4$, and NiFe$_2$O$_4$.

electron microscopy (SEM) images (Fig. S2). However, with the addition of Ni, the size of the ferrite particles gradually became larger, and the shape transformed to octahedral. Energy dispersive X-ray spectrum (EDX) mapping of NiFe$_2$O$_4$, Ni$_{0.5}$Co$_{0.5}$Fe$_2$O$_4$, and CoFe$_2$O$_4$ showed a uniform distribution of corresponding elements in all materials (Fig. 1a, S3a, b). Transmission electron microscopy (TEM) analysis, high resolution TEM (HRTEM) analysis, and fast Fourier transform (FFT) diagrams of NiFe$_2$O$_4$, Ni$_{0.5}$Co$_{0.5}$Fe$_2$O$_4$, and CoFe$_2$O$_4$ were carried out to further examine their morphology and composition. TEM images suggested that the size of CoFe$_2$O$_4$, Ni$_{0.5}$Co$_{0.5}$Fe$_2$O$_4$, and NiFe$_2$O$_4$ were ~20, 50, and 80 nm, respectively (Fig. 1b, S3c, d). The lattice fringes of CoFe$_2$O$_4$ displayed interplanar spacing of 0.486 nm (Fig. S3c), which matched well with the (111) plane of the CoFe$_2$O$_4$, while the lattice distance of (111) plane for NiFe$_2$O$_4$ is 0.483 nm (Fig. 1b). This may be due to the lattice distortion caused by Co replacing Ni. For Ni$_{0.5}$Co$_{0.5}$Fe$_2$O$_4$, the HRTEM image presented a clear lattice distance of 0.295 nm, corresponding to the (220) plane (Fig. S3d).

Raman scattering measurement of CoFe$_2$O$_4$, Ni$_{0.5}$Co$_{0.5}$Fe$_2$O$_4$, and NiFe$_2$O$_4$ were performed to confirm the lattice changes. As shown in Fig. 1c, five bands were observed, which were assigned to the vibrational modes of T$_{2g}$(III), E$_g$, T$_{2g}$(II), T$_{2g}$(I) and A$_{1g}$, respectively. These five modes can be attributed to the translational movement of the MO$_4$ (T$_{2g}$(III)), the symmetric bending of oxygen respected to the Fe^{3+} in Td sites (E$_g$), the asymmetric stretching of M-O binding in MO$_6$ (T$_{2g}$(II)), the vibrations of asymmetric bending of oxygen in Oh sites (T$_{2g}$(I)), and the symmetric stretching of O atoms from the M-O bonds at Td sites (A$_{1g}$) [34,35]. It was found that the T$_{2g}$(II), T$_{2g}$(III), and A$_{1g}$ bands shifted to the right sides with the addition of Ni, indicating the changes of vibrational frequency of the M-O bond at both Oh and Td positions. The Raman spectra confirmed that the introduction of Ni can change the lattice distortion degrees of Co$_{1-x}$Ni$_x$Fe$_2$O$_4$. Moreover, we conducted

Brunauer-Emmett-Teller (BET) analysis of different catalysts. As shown in Fig. 1d, the specific surface area (SA) of CoFe$_2$O$_4$ was 76.9 m^2/g. As the proportion of Ni increased, the SA decreased to 34.4 m^2/g for Ni$_{0.5}$Co$_{0.5}$Fe$_2$O$_4$ and to 27.2 m^2/g for NiFe$_2$O$_4$ (Fig. 1d).

Co$_{1-x}$Ni$_x$Fe$_2$O$_4$ with different compositions were then used as catalysts for the degradation of BPA over H$_2$O$_2$. Firstly, we determined the optimal pH and H$_2$O$_2$ dosage for the degradation experiments by comparing the BPA removal ratios under different reaction conditions (Fig. 2a, b). We found that NiFe$_2$O$_4$ showed the fastest removal ratio for BPA when H$_2$O$_2$ concentration was 20 mM and pH was 3.0. The pH value maintained during the degradation process (Fig. S4). Based on the Zeta potentials of BPA and NiFe$_2$O$_4$ at different pH values, the reason for the poor degradation performance of BPA at higher pH may be due to the mutual exclusion of charges between the catalyst and BPA (Fig. S5). As a result, these reaction parameters were adapted for all the BPA degradation experiments unless otherwise mentioned. The degradation profiles based of the change of the normalized concentration C/C$_0$ were displayed in Fig. 2c, the removal ratios of BPA increased with the increasing proportion of Ni, and NiFe$_2$O$_4$ exhibited the highest catalytic degradation activity (reaction rate constant (k) $\approx$ 0.023 min^{-1}) (Fig. S6). Two control experiments with only either NiFe$_2$O$_4$ or H$_2$O$_2$ dosage showed negligible degradation of BPA, indicating that the removal of BPA was resulted from the activation of H$_2$O$_2$ over the catalysts, other than the adsorption by NiFe$_2$O$_4$ or the sole oxidation by H$_2$O$_2$. Moreover, we compared the SA-normalized k of different catalysts and NiFe$_2$O$_4$ still demonstrated the highest activity (Fig. 2d). This result suggested that the difference regarding BPA removal ratios among these catalysts was not due to their difference in their SA.

Although NiFe$_2$O$_4$ demonstrated the highest catalytic performance, we noted that both Fe and Ni ions leaked during the reactions when NiFe$_2$O$_4$ was used as the catalyst (Fig. S7). The concentration of Fe ion in

Table 1
Bulk compositions determined by ICP, surface compositions, and the ratio of metal ion with different electronic structure determined by XPS.

	CoFe$_2$O$_4$	Ni$_{0.5}$Co$_{0.5}$Fe$_2$O$_4$	NiFe$_2$O$_4$
Bulk compositions	Co$_{0.999}$Fe$_2$O$_4$	Ni$_{0.533}$Co$_{0.527}$Fe$_2$O$_4$	Ni$_{0.991}$Fe$_2$O$_4$
Surface compositions	Co$_{0.899}$Fe$_2$O$_4$	Ni$_{0.495}$Co$_{0.467}$Fe$_2$O$_4$	Ni$_{1.31}$Fe$_2$O$_4$
Fe^{2+}/Fe^{3+}	0.17	0.16	0.16
Fe$^{3+}_{Oh}$/Fe$^{3+}_{Td}$	1.30	1.39	1.49
Ni^{2+}/Ni^{3+}	-	2.38	2.13
Co^{2+}/Co^{3+}	3.33	3.13	-
O$_{ads}$/O$_{total}$	0.23	0.35	0.35

the solution was below 0.2 mg/L (<0.05 wt‰ of the total iron in the catalyst) during the reaction, and the final concentration of Ni ion was ~0.8 mg/L (0.4 wt‰ of the total nickel in the catalyst). However, under the optimal reaction conditions, only Fe, Ni, or Fe coexisting with Ni with such concentrations were unable to demonstrate similar BPA removal ratios (Fig. S8), indicating that the catalytic performance of the studied ferrites was not resulted from the leakage of metal ions.

X-ray photoelectron spectroscopy (XPS) analysis was conducted to further analyze the surface cation oxidation states and chemical compositions of Co$_{1-x}$Ni$_x$Fe$_2$O$_4$ (Fig. S9). As shown in Table 1, compared with the bulk compositions determined by inductively coupled plasma (ICP) analysis, the surface atomic ratio of Co to Fe in CoFe$_2$O$_4$ determined by XPS was smaller, while the surface atomic ratio among Co, Ni to Fe in Ni$_{0.5}$Co$_{0.5}$Fe$_2$O$_4$ were close to that of the bulk. The atomic ratio of Ni to Fe on the surface of NiFe$_2$O$_4$ was much higher than that of the bulk, indicating that Ni tended to occupy surface sites. Moreover, the ratio between Co^{2+} and Co^{3+} or Ni^{2+} and Ni^{3+} of corresponding samples were relatively high, indicating that Co and Ni existed in a divalent form. However, when we substituted Co and Fe of the ferrites with Ni

completely and produced NiO, the latter showed little activity for BPA degradation (Fig. S10), suggesting that the higher performance of NiFe$_2$O$_4$ was not ascribed to the introduction of element Ni. The ratios between Fe^{2+} and Fe^{3+} of the three samples were close while the ratios of Fe^{3+} on the Oh to that on the Td sites (Fe$^{3+}_{Oh}$ and Fe$^{3+}_{Td}$) gradually increased with the increase of Ni content. However, a control experiment using Fe$_2$O$_3$, which only owned Fe$^{3+}_{Oh}$ in its structure, as the catalyst for H$_2$O$_2$ activation showed negligible degradation of BPA (Fig. S10). This result indicated that the different catalytic performance among the studied ferrites was not resulted from their electronic states of Fe. These results confirmed that the introduction of Ni was affecting the surface composition and electronic structure of the cations within the ferrites but was not responsible for the different catalytic performance of the studied ferrites.

In addition to the cations, we also analyzed the oxygen within the ferrites. The O 1 s peaks of the samples can be fitted into three peaks (Fig S8d), which were attributed to lattice oxygen (O$_{latt}$, 529.9 eV), surface absorbed oxygen (O$_{ads}$, 531.5 eV), and water molecules adsorbed on the surface (H$_2$O, 532.5 eV) [36,37]. Among all the three oxygen types, O$_{ads}$ is generally considered to be highly relevant to the surface O deficiency and plays a positive role in the Fenton-like process [38]. Quantitative analysis of oxygen species for the studied ferrites is shown in Fig. S8d and the proportions of O$_{ads}$ are also listed in Table 1. It was observed that the proportions of O$_{ads}$ in Ni$_{0.5}$Co$_{0.5}$Fe$_2$O$_4$ and NiFe$_2$O$_4$ were similar, but their catalytic performance varied greatly, indicating that O deficiency was neither the primary driving force of the activity difference among the ferrites.

In order to further explore the crystal structure changes of Ni$_x$Co$_{1-x}$Fe$_2$O$_4$ caused by composition regulation, we further analyzed the XRD patterns by using FullPROF program based on the Rietveld refinement method, which can give the refinement fitting parameters of
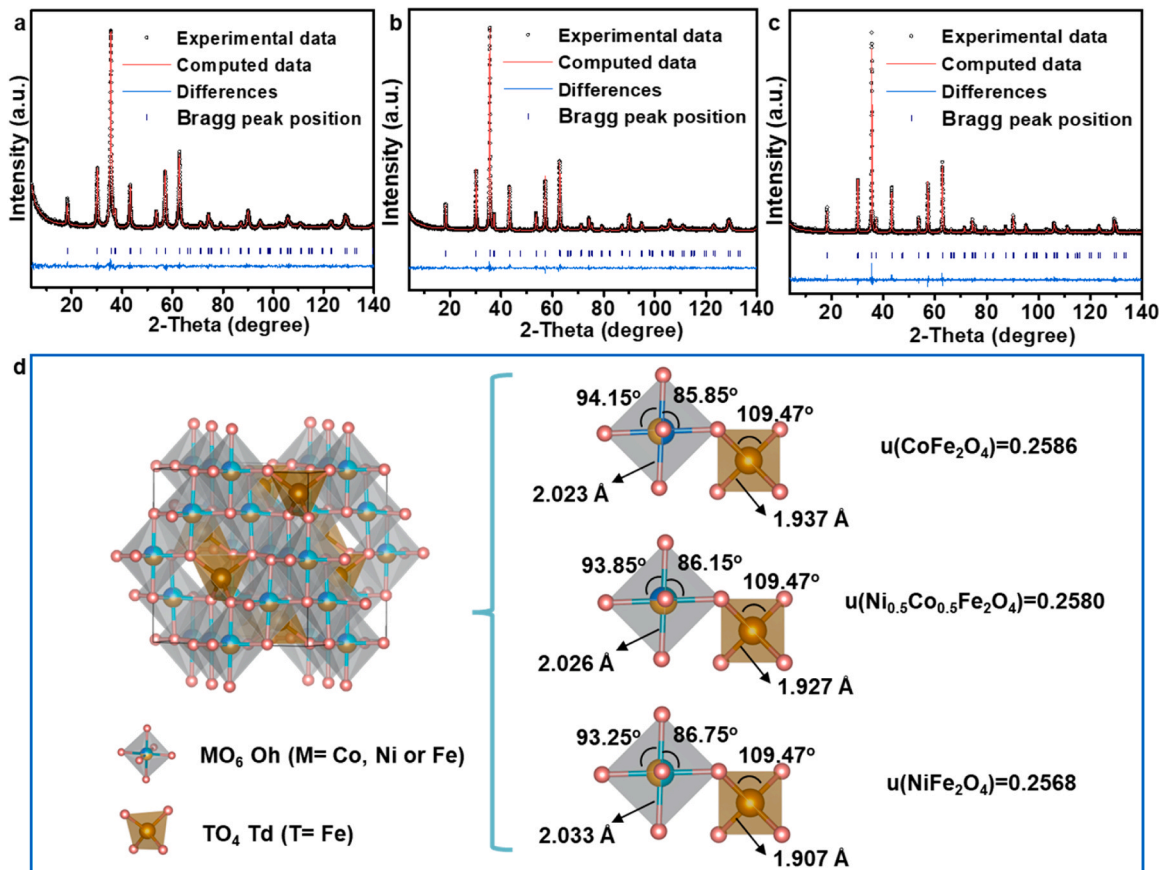

Fig. 3. Rietveld refined XRD profiles of (a) CoFe$_2$O$_4$, (b) Ni$_{0.5}$Co$_{0.5}$Fe$_2$O$_4$, and (c) NiFe$_2$O$_4$; (d) Structure diagram of Ni$_x$Co$_{1-x}$Fe$_2$O$_4$.

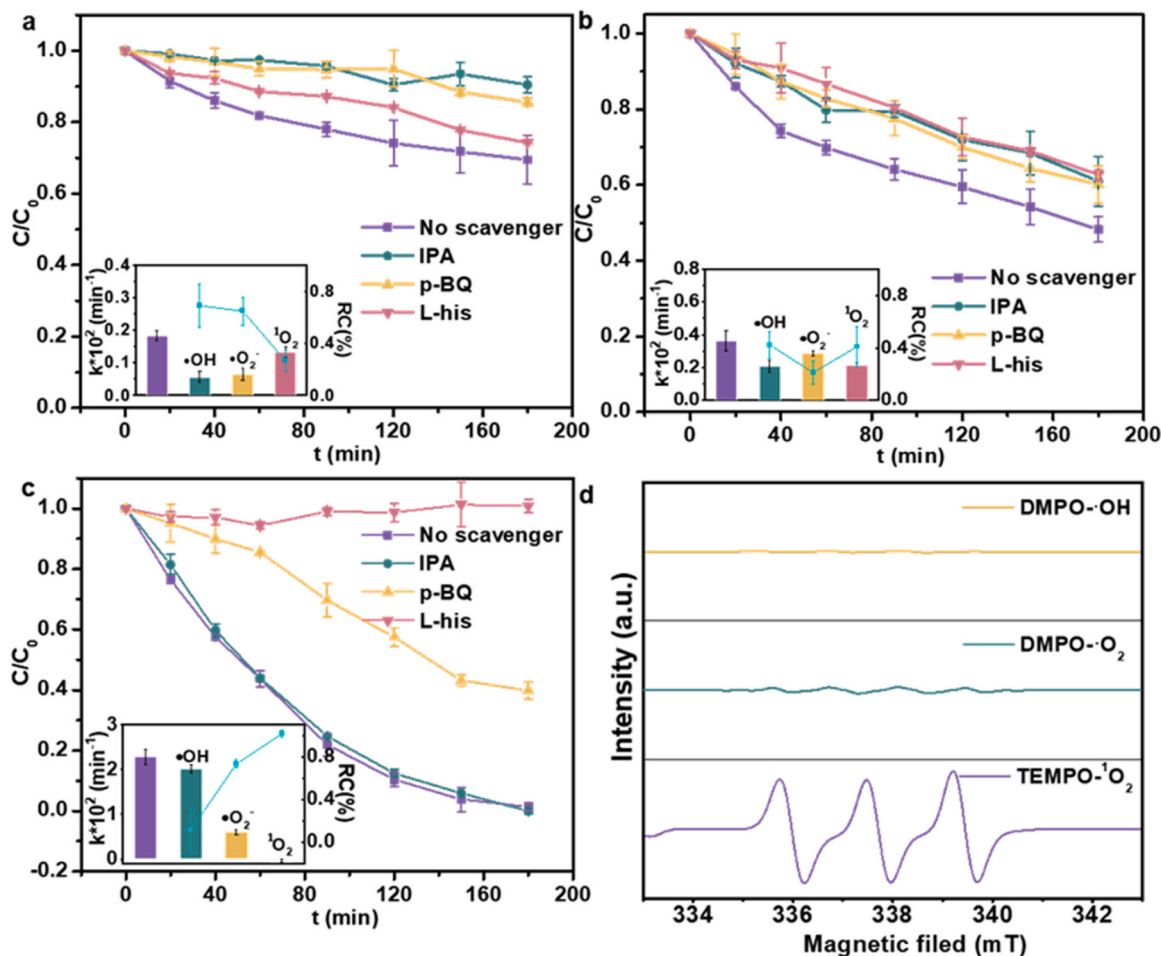**Fig. 4.** BPA degradation kinetics by H_2O_2 catalyzed by (a) $CoFe_2O_4$, (b) $Ni_{0.5}Co_{0.5}Fe_2O_4$, and (c) $NiFe_2O_4$ in the presence of different scavengers, the inset is the degradation kinetic rates and the RC of·OH and·O_2^-, $^1O_2$; (d) EPR spectra for •OH,·O_2^-, and $^1O_2$ in the $NiFe_2O_4/H_2O_2$ systems.

the different ferrites (Fig. 3a-c and Fig. S11). Table S2 presents the refinement fitting parameters, including lattice parameters and crystal structure for $Co_{1-x}Ni_xFe_2O_4$ ferrites. Structure diagrams of $Ni_xCo_{1-x}Fe_2O_4$ are shown in Fig. 3d and bond length, bond angle and oxygen parameter (u) for $CoFe_2O_4$, $Ni_{0.5}Co_{0.5}Fe_2O_4$, and $NiFe_2O_4$ are also marked in the Figure. The lattice distortion of the ferrites was determined by the changes regarding the bond length and angle. Since Ni^{2+} (0.69 Å) has smaller ionic radius than Co^{2+} (0.74 Å) [38], the introduction of Ni into $Ni_xCo_{1-x}Fe_2O_4$ decreased the lattice parameters and cell volume, indicating the contraction of lattice. The distortion of the spinel structure from ideal close-packing can be measured by u parameter, which can be calculated by the following Eqs. [39,40]:

$$M_{Td} - O = \sqrt{3}(u - \frac{1}{8})a \tag{9}$$

or

$$M_{Oh} - O = (3u^2 - 2u + \frac{3}{8})^{1/2}a \tag{10}$$

which M_{Td}-O and M_{Oh}-O represent the bond lengths of Td and Oh in spinel, respectively. We noted that with the substitution of Co with Ni, the u parameter decreased (Fig. 3d), indicating that the degree of lattice distortion decreased [41]. As the degree of lattice distortion decreases, the bond length of MO_6 Oh became longer while the bond length of MO_4 Td became shorter (Table S2, Fig. 3d). Consequently, the distortion of spinel ferrite structure can be effectively controlled by adjusting the ratio of Ni to Co. According to the analysis on the degree of lattice

distortion and catalytic performance, we found that when the degree of lattice distortion of the ferrites decreased, their corresponding catalytic activity increased.

3.2. Identification of ROS

To investigate the connection between the lattice distortion and catalytic performance of the ferrites, we firstly conducted ROS scavenging experiments to identify the major active species for BPA degradation over different ferrites. Herein, IPA, *p*-BQ and *L*-his were introduced to scavenge·OH,·O_2^- and $^1O_2$, respectively. It was observed that in the system of $CoFe_2O_4/H_2O_2$, the corresponding k value decreased from 0.0018 min^{-1} for the control experiment to 0.0006 min^{-1} for the experiment with IPA and *p*-BQ as the scavengers; the k value decreased to 0.0013 min^{-1} when *L*-his was used as the scavenger. It was estimated that the RC followed the order of·OH (68.8%) $\approx$ ·O_2^- (64.7%) $> ^1O_2$ (26.5%) (Fig. 4a, S12a). For $Ni_{0.5}Co_{0.5}Fe_2O_4$, each scavenger showed an obvious inhibition effect on BPA degradation, and the corresponding RC of·OH,·O_2^-, and $^1O_2$ for the degradation of BPA were estimated to be 42.3%, 21.2%, and 40.9%, respectively (Fig. 4c, S12b). Notably, the degradation efficiency significantly decreased with the addition of *p*-BQ and *L*-his as the scavengers in the $NiFe_2O_4/H_2O_2$ system. The corresponding k value decreased from 0.0228 min^{-1} to 0.0061 min^{-1} for *p*-BQ and to 0.0003 min^{-1} for *L*-his (Fig. 4c, S12c). Interestingly, the reaction was completely halted when *L*-his was spiked as the scavenger (Fig. 4c), indicating that $^1O_2$ might be the dominant ROS for the $NiFe_2O_4/H_2O_2$ system. Further estimation

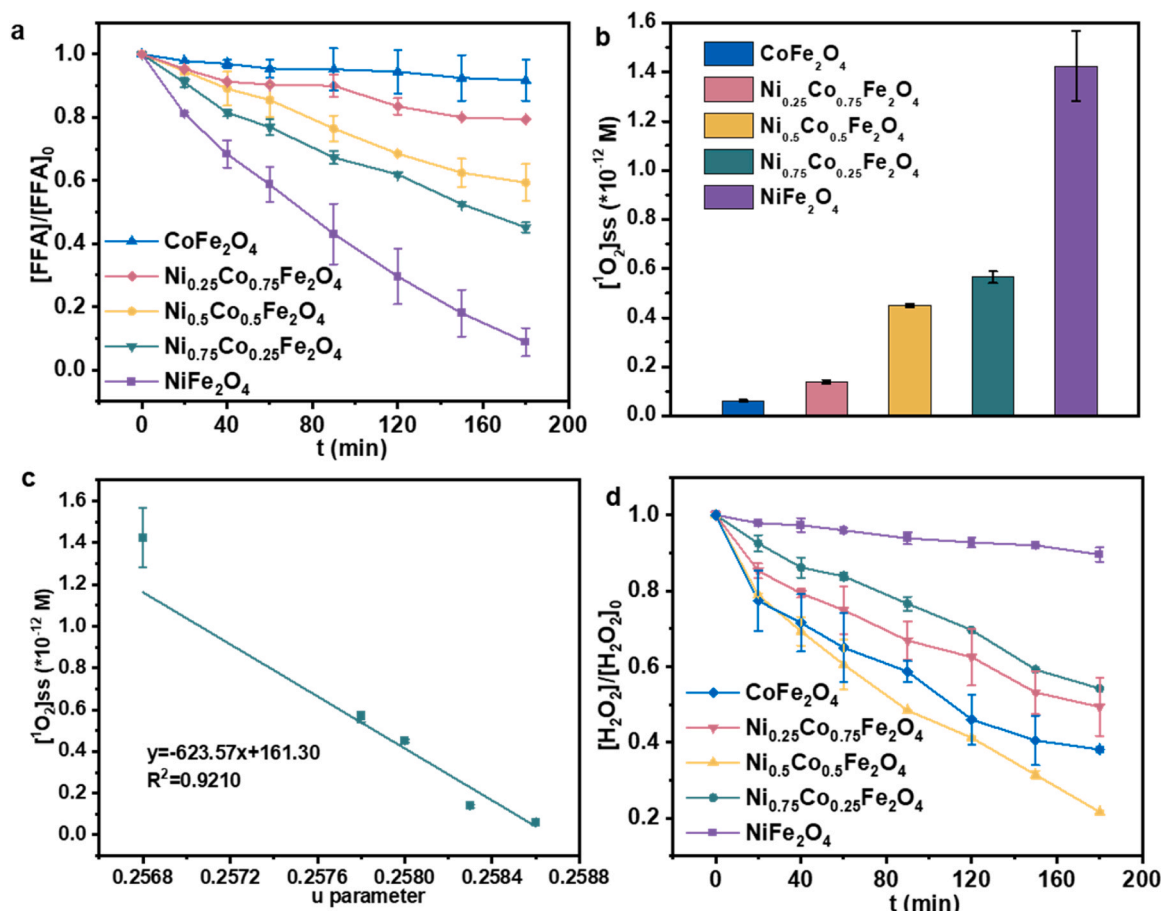**Fig. 5.** (a) The consumption of FFA in $NiFe_2O_4/H_2O_2$ system; (b) $[^1O_2]ss$ in the system; (c) The relationship between the generation of $^1O_2$ and the lattice distortion of $Ni_xCo_{1-x}Fe_2O_4$; (d) The change of H_2O_2 concentration during BPA degradation catalyzed by different catalyst.

suggested that the RC of $^1O_2$ for the degradation of BPA suggested was ~100%. Moreover, the addition of IPA had little effect on the BPA degradation efficiency, suggesting that·OH played practically no role for BPA degradation in the $NiFe_2O_4/H_2O_2$ system. As shown in the inset of Fig. 4c, the RC in the system of $NiFe_2O_4/H_2O_2$ followed the order of $^1O_2$ (100%) > $·O_2^-$ (73.3%) > >·OH (11.7%). In addition, we investigated the reaction between scavengers and H_2O_2 and found that these scavengers do not consume H_2O_2 (Fig. S13), which indirectly proved that quenching agents only quench ROS in these reaction systems.

To further identify the possible active species involved in the $NiFe_2O_4/H_2O_2$ system, we conducted EPR tests using DMPO and TEMP as spin-trapping agents. EPR results suggested that the $NiFe_2O_4/H_2O_2$ system can produce both·O_2^- and $^1O_2$, as their corresponding characteristic peaks were both observed (Fig. 4d). Scavenging experiments and EPR results collectively suggested that lattice distortion degrees of $Ni_xCo_{1-x}Fe_2O_4$ may affect the formation pathways of ROS: $CoFe_2O_4$, owning the highest lattice distortion degree, yielded the lowest amount of $^1O_2$ and demonstrated the lowest BPA removal ratio; on the contrary, $NiFe_2O_4$, owning the lowest lattice distortion degree, produced the highest amount of $^1O_2$ and demonstrated the highest BPA removal ratio.

The electron transfer process may play a role in the Fenton process, and electrochemical experiments were used to infer the role of electron transfer in the Fenton process. Cyclic voltammetry (CV) curves were measured to probe the oxidation potentials of BPA. As shown in Fig. S14a, an anodic oxidation peak of BPA appeared at~1.3 V during the CV scan in the BPA/Na_2SO_4 solution, indicating that BPA will be oxidized at this potential. Alternatively, by comparing the CV curves recorded in BPA/Na_2SO_4 and in Na_2SO_4 solution, we found that the onset potential for BPA oxidation was 1.23 V, which implied the starting

point for BPA oxidation. Then, the open-circuit potentials of $Ni_xCo_{1-x}Fe_2O_4$ were recorded in different solutions (Fig. S14b). The open-circuit potential of $CoFe_2O_4$, $Ni_{0.5}Co_{0.5}Fe_2O_4$ and $NiFe_2O_4$ in H_2O were ~0.81 V, 0.77 V and 0.72 V, respectively, there are no significant changes in the potentials after adding BPA. After continue adding H_2O_2 into the solutions, the open-circuit potential increased to 1.05 V, 1.09 V and 1.00 V, respectively. It may be due to the electron transfer from the $Ni_xCo_{1-x}Fe_2O_4$ to H_2O_2. However, these potentials were much lower than the onset oxidation potentials of BPA (1.23 V). Thus, the electron-transfer pathway could not directly oxidize BPA in $Ni_xCo_{1-x}Fe_2O_4/H_2O_2$ system.

FFA was employed as a molecular probe to estimate the steady-state concentrations of $^1O_2$ ($[^1O_2]ss$) during the Fenton-like reactions. As shown in Fig. 5a, the consumption of FFA in $NiFe_2O_4/H_2O_2$ system was the highest, indicating the highest $^1O_2$ production. The $[^1O_2]ss$ in the $Ni_xCo_{1-x}Fe_2O_4/H_2O_2$ systems are shown in Fig. 5b. The data show that there was a negative linear relationship between the u values of $Ni_xCo_{1-x}Fe_2O_4/H_2O_2$ and the $[^1O_2]ss$ (Fig. 5c), indicating a negative correlation between $^1O_2$ production and lattice distortion. According to consumption of FFA (Fig. 5a, S15), we calculated that the total amount of $^1O_2$ produced was ~0.175 ± 0.013 mM, ~0.049 ± 0.015 mM, and ~0 ± 0.013 mM for $NiFe_2O_4/H_2O_2$, $Ni_{0.5}Co_{0.5}Fe_2O_4/H_2O_2$, and $CoFe_2O_4/H_2O_2$, respectively. Moreover, as shown in Fig. S16, the yield of·OH in these systems followed the order of $Ni_{0.5}Co_{0.5}Fe_2O_4/H_2O_2$ (0.019 ± 0.002 mM) > $CoFe_2O_4/H_2O_2$ (0.011 ± 0.001 mM) > $Ni_{0.25}Co_{0.75}Fe_2O_4/H_2O_2$ (0.009 ± 0.001 mM) > $Ni_{0.75}Co_{0.25}Fe_2O_4/H_2O_2$ ≈ $NiFe_2O_4/H_2O_2$ (0.006 ± 0.001 mM), which was an order of magnitude lower than the yield of $^1O_2$. The low·OH production rates were consistent with the low BPA removal ratios for the systems using $Ni_{0.5}Co_{0.5}Fe_2O_4$ and $CoFe_2O_4$ as the catalysts. In addition,

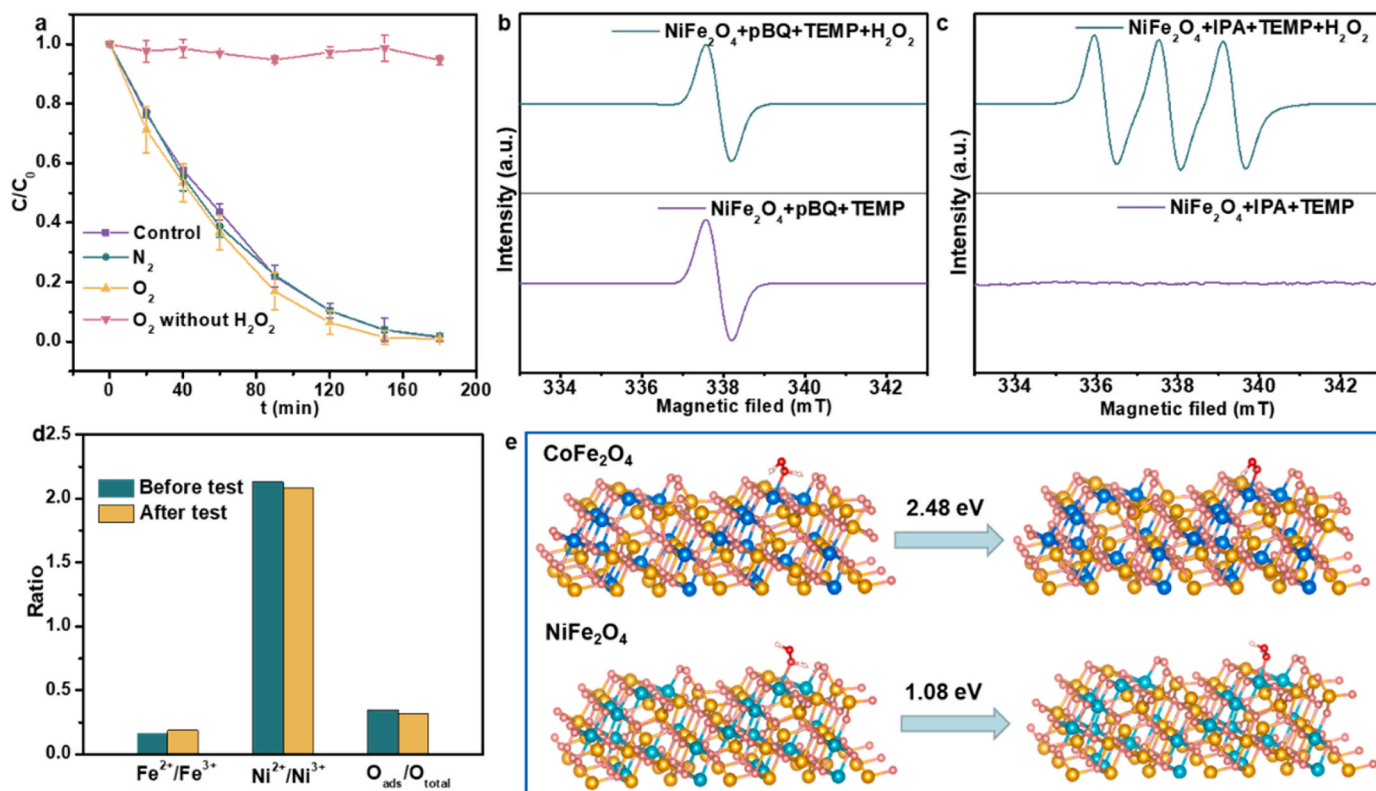**Fig. 6.** (a) Degradation of BPA by $NiFe_2O_4$ activated H_2O_2 under different atmospheres and without H_2O_2 under O_2 saturated atmosphere; (b) EPR spectra for the detection of $^1O_2$ in the presence of TEMP and *p*-BQ; (c) EPR spectra for the detection of $^1O_2$ in the presence of TEMP and IPA; (d) Quantitative analysis of different valence states of surface metals and different oxygen species detected by XPS; (e) Evolution process of H_2O_2 into •OOH on $CoFe_2O_4$ and $NiFe_2O_4$, atomic color: Co (blue), Fe (orange), O in spinel (pink), O in H_2O_2 (red), H (light pink), Ni (cyan).
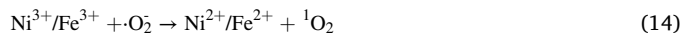
we noted that although the $NiFe_2O_4/H_2O_2$ system produced the highest amount of $^1O_2$ and demonstrated the fastest removal ratio of BPA, it consumed the the lowest amount of H_2O_2, accounting for only 10.3% of the total dosage when BPA was completely removed (Fig. 5d and S17). This result implied that $NiFe_2O_4$ was able to convert H_2O_2 to $^1O_2$ in an efficient way.

3.3. The mechanism of $^1O_2$ generation

Moreover, we studied the production pathway of $^1O_2$ in the $NiFe_2O_4/$ H_2O_2 system. It is widely recognized that for any Fenton-like systems, $^1O_2$ can be converted from primarily three sources:·OH,·O_2^- or O_2 [42–44]. As shown in Fig. 6a, neither N_2 nor O_2 purging impacted the removal ratio of BPA. Furthermore, when no H_2O_2 was added, BPA showed no degradation even when the solution was saturated in O_2, suggesting that the $^1O_2$ in the system was not derived from dissolved oxygen. The EPR signal of $^1O_2$ disappeared and the degradation efficiency of BPA decreased in the presence of *p*-BQ (Figs. 6b, 4c), indicating that·O_2^- affected the generation of $^1O_2$. On the contrary, the EPR signal of $^1O_2$ sustained and the degradation efficiency of BPA changed only a little in the presence of IPA (Figs. 6c, 4c), indicating that •OH had little influence on the generation of $^1O_2$. Above results collectively indicated that·O_2^- was the major source of $^1O_2$ in the $NiFe_2O_4/H_2O_2$ system.

The roles of Fe and Ni on the surface of $NiFe_2O_4$ in the Fenton-like reactions were investigated by comparing their chemical states before and after the reactions using XPS (Fig. S18). The ratio of Fe^{2+}/Fe^{3+}, Ni^{2+}/Ni^{3+} and O_{ads}/O_{latt} remained almost unchanged for $NiFe_2O_4$ before and after the reactions (Fig. 6d), indicating its satisfactory stability. Considering this fact, we proposed a mechanism for the $^1O_2$ production from H_2O_2 over $NiFe_2O_4$. Initially, Ni^{2+}/Fe^{2+} in $NiFe_2O_4$ break the O-H bond of H_2O_2 and convert it to·OOH (Eqs. 11, 12), which is further transforms into·O_2^- (Eq. 13). The electrons of·O_2^- are then

captured by Fe^{3+}/Ni^{3+} or·O_2^- reacts with other active species to produce $^1O_2$ (Eqs. 14–16).

$$Ni^{2+} + H_2O_2 \rightarrow Ni^{3+} + \cdot OOH + H^+ \qquad (11)$$

$$Fe^{2+} + H_2O_2 \rightarrow Fe^{3+} + \cdot OOH + H^+ \qquad (12)$$

$$\cdot OOH \leftrightarrow \cdot O_2^- + H^+ \qquad (13)$$

$$Ni^{3+}/Fe^{3+} + \cdot O_2^- \rightarrow Ni^{2+}/Fe^{2+} + {}^1O_2 \qquad (14)$$

$$\cdot OOH + \cdot O_2^- \rightarrow OOH^- + {}^1O_2 \qquad (15)$$

$$2 \cdot OOH \rightarrow {}^1O_2 + H_2O_2 \qquad (16)$$

Above speculation on the production pathway of $^1O_2$ allowed us to study the fundamental connections between the lattice distortion and their catalytic performance regarding H_2O_2 activation through DFT calculations. We used $NiFe_2O_4$ and $CoFe_2O_4$ as models to explore the free energy required for the conversion from H_2O_2 to the intermediate ·OOH, which has been considered as a key intermediate of $^1O_2$ production [12,45]. The theoretical model structures of $NiFe_2O_4$ or $CoFe_2O_4$ were constructed based on the (311) lattice plane, which is the primary one for the ferrites. For $NiFe_2O_4$, H_2O_2 is preferentially adsorbed on the Ni site because the adsorption energy of Ni site for H_2O_2 (−0.95 eV) is lower than that of Fe site (−0.76 eV), while the H_2O_2 adsorption is preferable on the Co site (−2.04 eV) for $CoFe_2O_4$ compared with Fe site (−0.81 eV) (Fig. S19). The higher adsorption energy of $CoFe_2O_4$ for H_2O_2 compared to $NiFe_2O_4$ may be due to the lattice distortion, which shortens the bond length of the metal-oxygen bond in Oh and enhances its covalence, thereby enhancing the adsorption of reactants and intermediate products [46,47]. Based on this preferential adsorption, we further calculated the energy required for the conversion from H_2O_2 to ·OOH on these two surfaces. For $CoFe_2O_4$, it requires
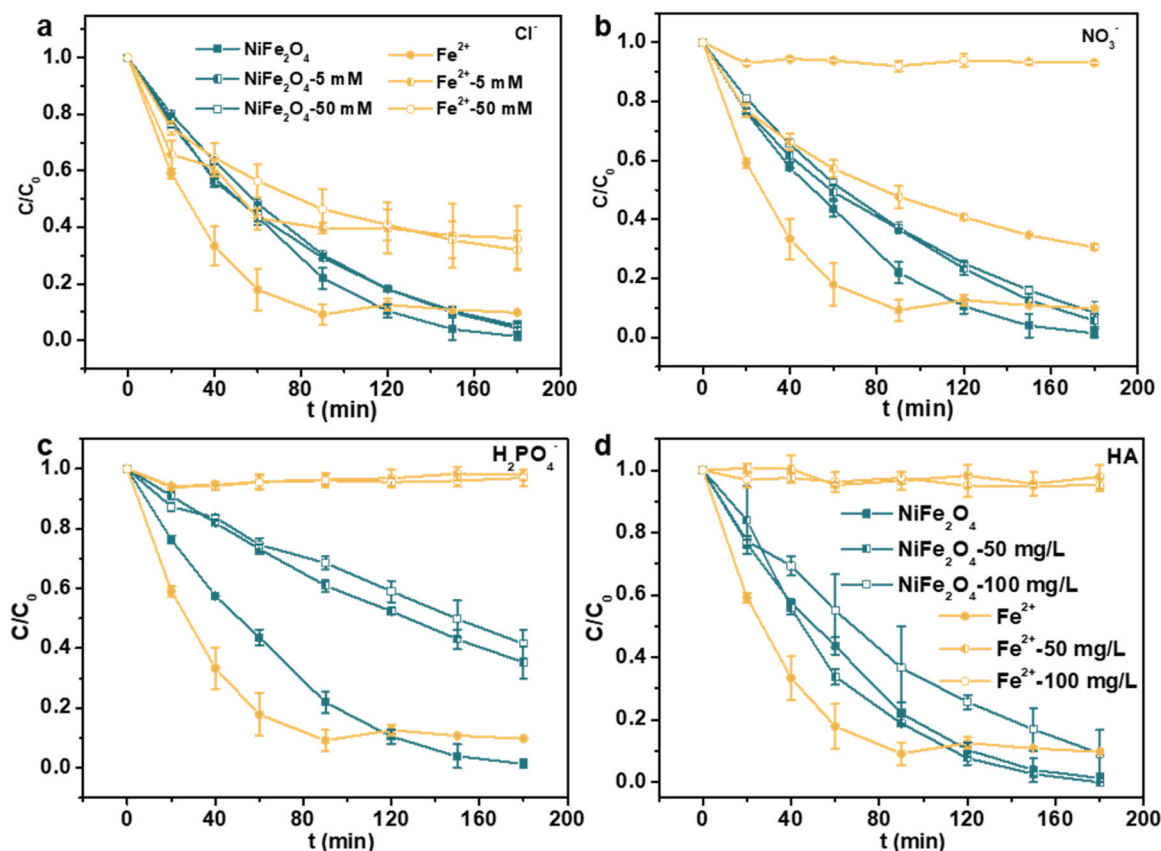
Fig. 7. Degradation kinetics of BPA by NiFe$_2$O$_4$/H$_2$O$_2$ (green line) and Fe^{2+}/H$_2$O$_2$ (yellow line) systems in the presence of (a) Cl$^-$, (b) NO$_3^-$, (c) H$_2$PO$_4^-$, (d) HA with different concentrations. Experimental conditions for Fe^{2+}/H$_2$O$_2$: c(Fe^{2+})= 0.02 mM, c(H$_2$O$_2$)= 4 mM, pH= 3.0. Under such condition, the removal ratio of BPA was close to that in the NiFe$_2$O$_4$/H$_2$O$_2$ system when no interfering components were dosed.

2.48 eV of energy to break the bonds of H$_2$O$_2$ to form ·OOH, while that for NiFe$_2$O$_4$ is only 1.08 eV (Fig. 6e). This may be due to the different local microenvironment of catalysis caused by lattice distortion, which makes the bond length of O-H of H$_2$O$_2$ in NiFe$_2$O$_4$/H$_2$O$_2$ system (1.044 Å) longer than that of in CoFe$_2$O$_4$/H$_2$O$_2$ system (1.031 Å) [48]. Thus, NiFe$_2$O$_4$ is more effective for H$_2$O$_2$ activation to generate intermediate products and further produce ^{1}O$_2$, as compared to CoFe$_2$O$_4$. Therefore, we concluded that the preferential generation of ^{1}O$_2$ can be achieved by rational tuning of the lattice distortion of Co$_{1-x}$Ni$_x$Fe$_2$O$_4$.

3.4. Advantages of NiFe$_2$O$_4$/H$_2$O$_2$ system

As a non-radical ROS, ^{1}O$_2$ is highly selective to pollutants with electron-donating groups, while it shows little oxidation capacity for pollutants that do not contain these groups [17,49,50]. Consistently, the NiFe$_2$O$_4$/H$_2$O$_2$ system was ineffective (~4% in 180 min) in BA degradation, which is a pollutant without electron-donating groups (Fig. S20). Moreover, ^{1}O$_2$ is considered to have lower reactivity with water components compared with target pollutants with electron rich group [9,42, 50]. Indeed, when 50 mM (500 times higher concentration that that of BPA) of Cl$^-$ or NO$_3^-$ was spiked into the NiFe$_2$O$_4$/H$_2$O$_2$ system, it showed negligible effect on BPA degradation kinetics (Fig. 7a, b). On the contrary, in the conventional Fenton system (Fe^{2+}/H$_2$O$_2$), which is primarily dependent on ·OH, the BPA degradation was significantly quenched in the presence of the above-mentioned water components. For example, 5 mM of NO$_3^-$ inhibited the reaction rate by ~40% and 50 mM of NO$_3^-$ totally halted the reaction. It was also noted that 50 mM of H$_2$PO$_4^-$ decreased the BPA removal ratio even in the NiFe$_2$O$_4$/H$_2$O$_2$ system by ~ 40% (Fig. 7c), possibly because H$_2$PO$_4^-$ has a strong affinity for the surface hydroxyl groups on heterogeneous catalysts and

competed with BPA for the active sites [51,52]. Regardless, the inhibition effect of H$_2$PO$_4^-$ on BPA degradation over ^{1}O$_2$ in NiFe$_2$O$_4$/H$_2$O$_2$ system was significantly lower than that over·OH in the Fenton system. Moreover, in the presence of HA, the reaction of Fe^{2+}/H$_2$O$_2$ was completely inhibited, while NiFe$_2$O$_4$/H$_2$O$_2$ system was less affected, indicating that ^{1}O$_2$ is highly selective to the target pollutant. Moreover, the interference of ions on the CoFe$_2$O$_4$/H$_2$O$_2$ was also investigated. As shown in Fig. S21, the degradation rate of BPA was inhibited significantly only at a concentration of 5 mM of anions and 50 mg/L HA. Therefore, we can conclude that NiFe$_2$O$_4$/H$_2$O$_2$ system has good selectivity and shows strong resistance to ion interference.

In addition, as mentioned earlier, the transformation efficiency from H$_2$O$_2$ to ^{1}O$_2$ for NiFe$_2$O$_4$ was high. To demonstrate this advantage, we compared the reuse cycle performance of different Fenton-like systems, including nZVI/H$_2$O$_2$, Fe^{2+}/H$_2$O$_2$, CoFe$_2$O$_4$/H$_2$O$_2$, and NiFe$_2$O$_4$/H$_2$O$_2$ systems by spiking fresh BPA after each reuse cycle. As shown in Fig. 8, BPA can be completely degraded by nZVI/H$_2$O$_2$, Fe^{2+}/H$_2$O$_2$ and NiFe$_2$O$_4$/H$_2$O$_2$ within 4 h, while the degradation efficiency of CoFe$_2$O$_4$/H$_2$O$_2$ reached 20% for the first cycle. After spiking fresh BPA again, the NiFe$_2$O$_4$/H$_2$O$_2$ system still demonstrated the same performance for five consecutive reuse cycles, while the degradation efficiency of other systems decreased. Although the initial BPA concentrations varied among different systems from the 2nd cycle, due to their different BPA removal ratio in the previous cycle, the results clearly indicated the satisfactory performance of NiFe$_2$O$_4$/H$_2$O$_2$ over a long term.

4. Conclusion

In summary, we demonstrated that through the manipulation of the lattice distortion of Co$_{1-x}$Ni$_x$Fe$_2$O$_4$ via adjusting the Ni content, the

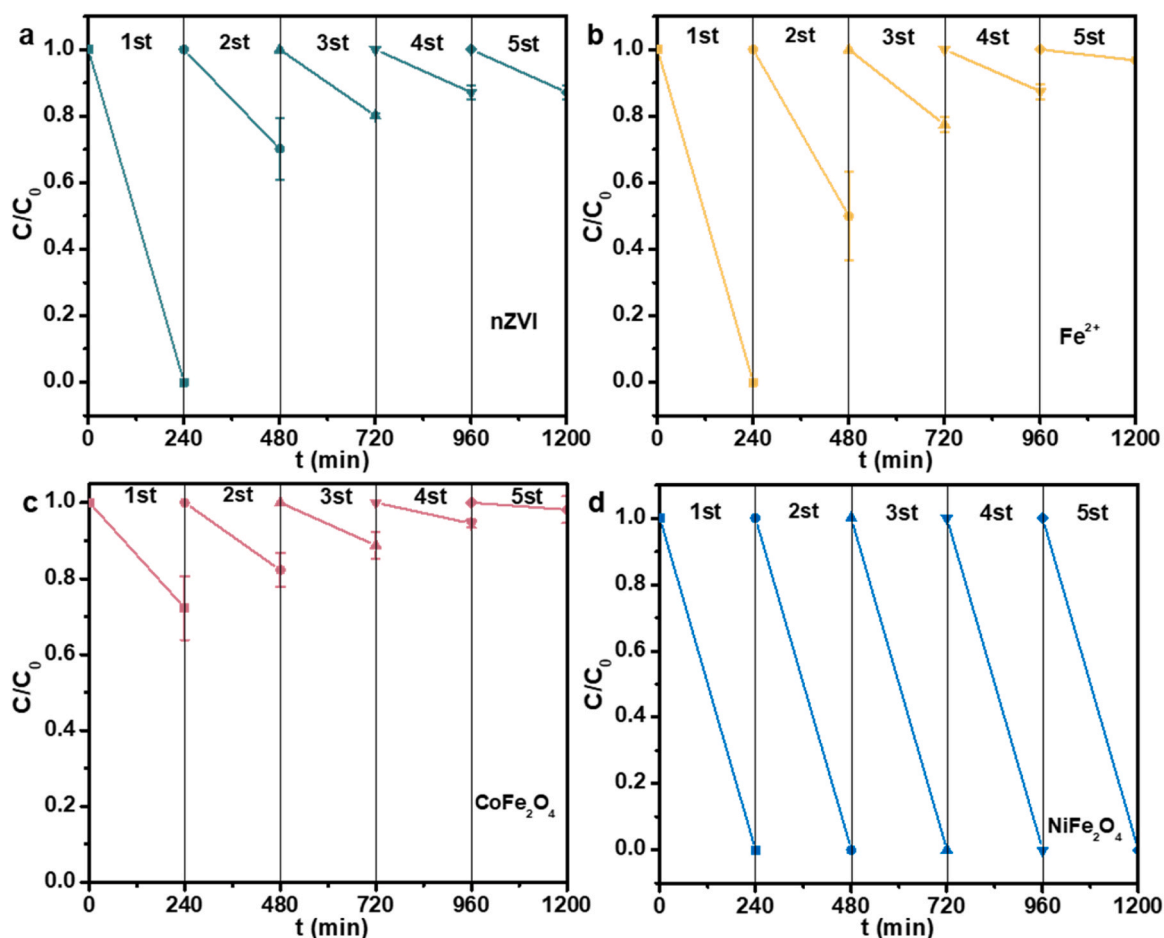**Fig. 8.** The reuse cycle performance of (a) nZVI/H_2O_2, (b) Fe/ H_2O_2, (c) $CoFe_2O_4$/H_2O_2 and (d) $NiFe_2O_4$/H_2O_2 system. Between each reuse cycle, fresh BPA solution was spiked into the systems. Experimental conditions for nZVI/H_2O_2, $CoFe_2O_4$/H_2O_2 and $NiFe_2O_4$/H_2O_2 system: c(catalyst) = 0.2 g/L, c(H_2O_2)= 10 mM, pH= 3.0; Experimental conditions for Fe^{2+}/H_2O_2: c(Fe^{2+})= 0.02 mM, c(H_2O_2)= 4 mM, pH= 3.0.

production pathway of ROS from H_2O_2 can be controlled. With the increase of Ni content, the lattice distortion decreased and the ability of the ferrites to activate H_2O_2 changed. Because of this difference, the dominant ROS generated during the degradation reactions changed from ·OH for $CoFe_2O_4$ to $^1O_2$ for $NiFe_2O_4$, as verified by scavenging experiments and EPR results. Further experiments verified that $^1O_2$ was converted from ·O_2^- in the $NiFe_2O_4$/H_2O_2 system. DFT calculations revealed that the underlying connection between the lattice distortion and ROS production pathway was resulted from the lower free energy required for $NiFe_2O_4$ to decompose H_2O_2, as compared to $CoFe_2O_4$, which owned a higher lattice distortion degree. Compared to the conventional Fenton process, which is primarily dependent on ·OH, the $NiFe_2O_4$/H_2O_2 system showed selectivity towards the degradation of target pollutant in the presence of interfering water components. It is also noteworthy that $NiFe_2O_4$ was able to convert H_2O_2 to $^1O_2$ efficiently, consuming ∼ 10% of H_2O_2 when 0.1 mM of BPA was totally removed. $NiFe_2O_4$/H_2O_2 system was effective and completely removed BPA over 5 consecutive reuse cycles without dosing any fresh H_2O_2. Our work suggests that the conversion efficiency and formation pathway of $^1O_2$ from H_2O_2 can be regulated by rational design of ferrite catalysts, which is of practical importance considering the Fenton-like reactions are widely used in water treatment applications.

CRediT authorship contribution statement

Yilan Jiang: Conceptualization, Methodology, Writing – original draft preparation, Writing – review & editing. **Peifang Wang:** Supervision, Funding acquisition, Writing – review & editing. **Tingyue Chen:** Formal analysis. **Keyi Gao:** Data curation. **Yiran Xiong:** Validation; **Dionysios D. Dionysiou:** Supervision, Writing – review & editing. **Dawei Wang:** Supervision, Writing – review & editing, Project administration, Funding acquisition.

Declaration of Competing Interest

The authors declare that they have no known competing financial interests or personal relationships that could have appeared to influence the work reported in this paper.

Data Availability

Data will be made available on request.

Acknowledgement

Appendix A. Supporting information

Supplementary data associated with this article can be found in the online version at doi:10.1016/j.apcatb.2023.123468.

References

[1] B. Song, Z. Zeng, E. Almatrafi, M. Shen, W. Xiong, C. Zhou, W. Wang, G. Zeng, J. Gong, Pyrite-mediated advanced oxidation processes: applications, mechanisms, and enhancing strategies, Water Res 211 (2022), 118048, https://doi.org/10.1016/j.watres.2022.118048.

[2] Y. Zhu, R. Zhu, Y. Xi, J. Zhu, G. Zhu, H. He, Strategies for enhancing the heterogeneous Fenton catalytic reactivity: a review, Appl. Catal. B-Environ. 255 (2019), 117739, https://doi.org/10.1016/j.apcatb.2019.05.041.

[3] C. Walling, Fenton's reagent revisited, Acc. Chem. Res 8 (1975) 125–131, https://doi.org/10.1021/ar50088a003.

[4] J.J. Pignatello, E. Oliveros, A. MacKay, Advanced oxidation processes for organic contaminant destruction based on the Fenton reaction and related chemistry, Crit. Rev. Environ. Sci. Technol. 36 (2006) 1–84, https://doi.org/10.1080/10643380500326564.

[5] S. Enami, Y. Sakamoto, A.J. Colussi, Fenton chemistry at aqueous interfaces, Proc. Natl. Acad. Sci. USA 111 (2014) 623–628, https://doi.org/10.1073/pnas.131488511.

[6] Z.G. Zhou, H.M. Du, Z. Dai, Y. Mu, L.L. Tong, Q.J. Xing, S.S. Liu, Z. Ao, J.P. Zou, Degradation of organic pollutants by peroxymonosulfate activated by MnO_2 with different crystalline structures: catalytic performances and mechanisms, Chem. Eng. J. 374 (2019) 170–180, https://doi.org/10.1016/j.cej.2019.05.170.

[7] L. Zhang, Y. Sun, R. Ge, W. Zhou, Z. Ao, J. Wang, Mechanical insight into direct singlet oxygen generation pathway: pivotal role of FeN4 sites and selective organic contaminants removal, Appl. Catal. B-Environ. 339 (2023), 123130, https://doi.org/10.1016/j.apcatb.2023.12313.

[8] G. Wang, S. Chen, X. Quan, H. Yu, Y. Zhang, Enhanced activation of peroxymonosulfate by nitrogen doped porous carbon for effective removal of organic pollutants, Carbon 115 (2017) 730–739, https://doi.org/10.1016/j.carbon.2017.01.060.

[9] R. Luo, M. Li, C. Wang, M. Zhang, M.A.N. Khan, X. Sun, J. Shen, W. Han, L. Wang, J. Li, Singlet oxygen-dominated non-radical oxidation process for efficient degradation of bisphenol A under high salinity condition, Water Res 148 (2019) 416–424, https://doi.org/10.1016/j.watres.2018.10.087.

[10] Y. Wang, Y. Lin, S. He, S. Wu, C. Yang, Singlet Oxygen: Properties, Generation, Detection, and Environmental Applications, J. Hazard. Mater. 461 (2023), 132538, https://doi.org/10.1016/j.jhazmat.2023.132538.

[11] D. Wang, A.L. Junker, M. Sillanpää, Y. Jiang, Z. Wei, Photo-based Advanced Oxidation Processes for Zero Pollution: Where Are We Now? Engineering 23 (2023) 19–23, https://doi.org/10.1016/j.eng.2022.08.005.

[12] Z. Yang, J. Qian, A. Yu, B. Pan, Singlet oxygen mediated iron-based Fenton-like catalysis under nanoconfinement, Proc. Natl. Acad. Sci. USA 116 (2019) 6659–6664, https://doi.org/10.1073/pnas.1819382116.

[13] Q. Yi, J. Ji, B. Shen, C. Dong, J. Liu, J. Zhang, M. Xing, Singlet oxygen triggered by superoxide radicals in a molybdenum cocatalytic fenton reaction with enhanced REDOX activity in the environment, Environ. Sci. Technol. 53 (2019) 9725–9733, https://doi.org/10.1021/acs.est.9b01676.

[14] A.G. Leonel, A.A.P. Mansur, H.S. Mansur, Advanced functional nanostructures based on magnetic iron oxide nanomaterials for water remediation: a review, Water Res. 190 (2021) 116693, https://doi.org/10.1016/j.watres.2020.116693.

[15] Y. Yin, Y. Zhang, B. Wu, L. Hu, Y. Wang, J. Wan, W. Zhang, Facet-dependent reactivity of α-Fe_2O_3 nanosheet on reactive oxygen species generation in Fenton-like process, Appl. Catal. B-Environ. (2023), 123165, https://doi.org/10.1016/j.apcatb.2023.123165.

[16] L.-S. Zhang, X.-H. Jiang, Z.-A. Zhong, L. Tian, Q. Sun, Y.-T. Cui, X. Lu, J.-P. Zou, S.-L. Luo, Carbon Nitride Supported High-Loading Fe Single-Atom Catalyst for Activating of Peroxymonosulfate to Generate $^1O_2$ with 100% Selectivity, Angew. Chem. Int. Ed. 60 (2021) 21751–21755, https://doi.org/10.1002/anie.202109488.

[17] Y. Yao, C. Wang, X. Yan, H. Zhang, C. Xiao, J. Qi, Z. Zhu, Y. Zhou, X. Sun, X. Duan, J. Li, Rational regulation of Co-N-C coordination for high-efficiency generation of $^1O_2$ toward nearly 100% selective degradation of organic pollutants, Environ. Sci. Technol. 56 (2022) 8833–8843, https://doi.org/10.1021/acs.est.2c00706.

[18] T. Tatarchuk, A. Shyichuk, I. Trawczynska, I. Yaremiy, A.T. Pedziwiatr, P. Kurzydlo, B.F. Bogacz, R. Gargula, Spinel cobalt(II) ferrite-chromites as catalysts for H_2O_2 decomposition: synthesis, morphology, cation distribution and antistructure model of active centers formation, Ceram. Int. 46 (2020) 27517–27530, https://doi.org/10.1016/j.ceramint.2020.07.243.

[19] F. Sharifianjazi, M. Moradi, N. Parvin, A. Nemati, A.J. Rad, N. Sheysi, A. Abouchenari, A. Mohammadi, S. Karbasi, Z. Ahmadi, A. Esmaeilkhanian, M. Irani, A. Pakseresht, S. Sahmani, M.S. Asl, Magnetic $CoFe_2O_4$ nanoparticles doped with metal ions: a review, Ceram. Int. 46 (2020) 18391–18412, https://doi.org/10.1016/j.ceramint.2020.04.202.

[20] F. Cheng, J. Shen, B. Peng, Y. Pan, Z. Tao, J. Chen, Rapid room-temperature synthesis of nanocrystalline spinels as oxygen reduction and evolution electrocatalysts, Nat. Chem. 3 (2011) 79–84, https://doi.org/10.1038/NCHEM.931.

[21] R.C. Peterson, G.A. Lager, R.L. Hitterman, A time-of-flight neutron powder diffraction study of $MgAl_2O_4$ at temperatures up to 1273 K, Am. Miner. 76 (1991) 1455–1458, https://doi.org/10.1016/j.micinf.2008.11.003.

[22] R.J. Hill, J.R. Craig, G.V. Gibbs, Systematics of the spinel structure type, Phys. Chem. Miner. 4 (1979) 317–339, https://doi.org/10.1007/BF00307535.

[23] M. Qanbarzadeh, D. Wang, M. Ateia, S.P. Sahu, E.L. Cates, Impacts of reactor configuration, degradation mechanisms, and water matrices on perfluorocarboxylic acid treatment efficiency by the UV/$Bi_3O(OH)(PO_4)_2$ photocatalytic process, ACS EST Eng. 1 (2020) 239–248, https://doi.org/10.1021/acsestengg.0c00086.

[24] F. Xu, C. Lai, M. Zhang, B. Li, L. Li, S. Liu, D. Ma, X. Zhou, H. Yan, X. Hou, B. Wang, H. Yi, L. Qin, L. Tang, High-loaded single-atom Cu-N_3 sites catalyze hydrogen peroxide decomposition to selectively induce singlet oxygen production for wastewater purification, Appl. Catal. B-Environ. 339 (2023), 123075, https://doi.org/10.1016/j.apcatb.2023.123075.

[25] Y. Mu, G. Zhan, C. Huang, X. Wang, Z. Ai, J. Zou, S. Luo, L. Zhang, Dechlorination-hydroxylation of atrazine to hydroxyatrazine with thiosulfate: a detoxification strategy in seconds, Environ. Sci. Technol. 53 (2019) 3208–3216, https://doi.org/10.1021/acs.est.8b06351.

[26] H. Che, P. Wang, J. Chen, X. Gao, B. Liu, Y. Ao, Rational design of donor-acceptor conjugated polymers with high performance on peroxydisulfate activation for pollutants degradation, Appl. Catal. B-Environ. 316 (2022), 121611, https://doi.org/10.1016/j.apcatb.2022.121611.

[27] R.M. Dalrymple, A.K. Carfagno, C.M. Sharpless, Correlations between dissolved organic matter optical properties and quantum yields of singlet oxygen and hydrogen peroxide, Environ. Sci. Technol. 44 (2010) 5824–5829, https://doi.org/10.1021/es101005u.

[28] J.R. Laszakovits, S.M. Berg, B.G. Anderson, J.E. O'Brien, K.H. Wammer, C. M. Sharpless, p-nitroanisole/pyridine and p-nitroacetophenone/pyridine actinometers revisited: quantum yield in comparison to ferrioxalate, Environ. Sci. Technol. Lett. 4 (2017) 11–14, https://doi.org/10.1021/acs.estlett.6b00422.

[29] J. Jiang, S. Liu, D. Shi, T. Sun, Y. Wang, S. Fu, Y. Liu, M. Li, D. Zhou, S. Dong, Spin state-dependent in-situ photo-Fenton-like transformation from oxygen molecule towards singlet oxygen for selective water decontamination, Water Res. 244 (2023), 120502, https://doi.org/10.1016/j.watres.2023.120502.

[30] M. Linetsky, B.J. Ortwerth, Quantitation of the singlet oxygen produced by UVA irradiation of human lens proteins, Photochem. Photobiol. 65 (1997) 522–529, https://doi.org/10.1111/j.1751-1097.1997.tb08598.x.

[31] S.H. Joo, A.J. Feitz, D.L. Sedlak, T.D. Waite, Quantification of the oxidizing capacity of nanoparticulate zero-valent iron, Environ. Sci. Technol. 39 (2005) 1263–1268, https://doi.org/10.1021/es048983d.

[32] K. Mopper, X. Zhou, Hydroxyl radical photoproduction in the sea and its potential impact on marine processes, Science 250 (1990) 661–664, https://doi.org/10.1126/science.250.4981.661.

[33] P. Chen, Y. Mu, Y. Chen, L. Tian, X.H. Jiang, J.P. Zou, S.L. Luo, Shifts of surface-bound• OH to homogeneous• OH in BDD electrochemical system via UV irradiation for enhanced degradation of hydrophilic aromatic compounds, Chemosphere 291 (2022), 132817, https://doi.org/10.1016/j.chemosphere.2021.132817.

[34] L.V. Gasparov, D.B. Tanner, D.B. Romero, H. Berger, G. Margaritondo, L. Forro, Infrared and Raman studies of the Verwey transition in magnetite, Phys. Rev. B 62 (2000) 7939–7944, https://doi.org/10.1103/PhysRevB.62.7939.

[35] A. Kumar, P. Sharma, D. Varshney, Structural, vibrational and dielectric study of Ni doped spinel Co ferrites: $Co_{1-x}Ni_xFe_2O_4$ (x=0.0, 0.5, 1.0), Ceram. Int 40 (2014) 12855–12860, https://doi.org/10.1016/j.ceramint.2014.04.140.

[36] Y. Jiang, Z. Geng, L. Yuan, Y. Sun, Y. Cong, K. Huang, L. Wang, W. Zhang, Nanoscale Architecture of RuO_2/$La_{0.9}Fe_{0.92}Ru_{0.08-x}O_{3-delta}$ Composite via Manipulating the Exsolution of Low Ru-Substituted A-Site Deficient Perovskite, ACS Sustain. Chem. Eng. 6 (2018) 11999–12005, https://doi.org/10.1021/acssuschemeng.8b02288.

[37] M.J. Kang, H. Park, J. Jegal, S.Y. Hwang, Y.S. Kang, H.G. Cha, Electrocatalysis of 5-hydroxymethylfurfural at cobalt based spinel catalysts with filamentous nanoarchitecture in alkaline media, Appl. Catal. B-Environ. 242 (2019) 85–91, https://doi.org/10.1016/j.apcatb.2018.09.087.

[38] M.A. Younis, S. Lyu, C. Lei, B. Yang, Z. Li, Q. He, J. Lu, L. Lei, Y. Hou, Efficient mineralization of sulfanilamide over oxygen vacancy-rich NiFe-LDH nanosheets array during electro-fenton process, Chemosphere 268 (2021), 129272, https://doi.org/10.1016/j.chemosphere.2020.129272.

[39] F. Bosi, Chemical and structural variability in cubic spinel oxides, Acta Crystallogr. B 75 (2019) 279–285, https://doi.org/10.1107/S2052520619002282.

[40] Y. Kudoh, T. Kuribayashi, H. Mizobata, E. Ohtani, S. Sasaki, M. Tanaka, Pressure dependence of u parameter in ringwoodite up to 7.9 GPa, J. Miner. Petro. Sci. 102 (2007) 8–11, https://doi.org/10.2465/jmps.060316.

[41] K. Robinson, G.V. Gibbs, P.H. Ribbe, Quadratic elongation: a quantitative measure of distortion in coordination polyhedra, Science 172 (1971) 567–570, https://doi.org/10.1126/science.172.3983.5.

[42] D. Wang, M. Angel Mueses, J.A. Colina Marquez, F. Machuca-Martinez, I. Grcic, R. P. Muniz Moreira, G. Li Puma, Engineering and modeling perspectives on photocatalytic reactors for water treatment, Water Res 202 (2021), 117421, https://doi.org/10.1016/j.watres.2021.117421.

[43] Z. Huang, Z. Shanmugam, Z. Liu, A. Brookfield, E.L. Bennett, R. Guan, D.E. V. Herrera, J.A. Lopez-Sanchez, A.G. Slater, E.J.L. McInnes, X. Qi, J. Xiao, Chemical Recycling of Polystyrene to Valuable Chemicals via Selective Acid-Catalyzed Aerobic Oxidation under Visible Light, J. Am. Chem. Soc. 144 (2022) 6532–6542, https://doi.org/10.1021/jacs.2c01410.

[44] T. Kanti Das, M.R. Wati, K. Fatima-Shad, Oxidative Stress Gated by Fenton and Haber Weiss Reactions and Its Association With Alzheimer's Disease, Arch. Neurosci. 2 (No. e60038) (2014), https://doi.org/10.5812/archneurosci.20078.

[45] Q. Yi, J. Ji, B. Shen, C. Dong, J. Liu, J. Zhang, M. Xing, Singlet Oxygen Triggered by Superoxide Radicals in a Molybdenum Cocatalytic Fenton Reaction with Enhanced REDOX Activity in the Environment, Environ. Sci. Technol. 53 (2019) 9725–9733, https://doi.org/10.1021/acs.est.9b01676.

[46] C. Ye, H. Cheng, L. Zheng, J. Lin, Q. Xu, Y. Qiu, Z. Pan, Y. Qiu, Tailoring metal-oxygen bonds boosts oxygen reaction kinetics for high-performance zinc-air batteries, Nano Lett. 23 (2023) 1573–1581, https://doi.org/10.1021/acs.nanolett.3c00053.

[47] J. Zaffran, M.C. Toroker, Metal-oxygen bond ionicity as an efficient descriptor for doped niooh photocatalytic activity, Chemphyschem 17 (2016) 1630–1636, https://doi.org/10.1002/cphc.201600049.

[48] X. Xu, Y. Zhang, Y. Chen, C. Liu, W. Wang, J. Wang, H. Huang, J. Feng, Z. Li, Z. Zou, Revealing *OOH key intermediates and regulating H_2O_2 photoactivation by surface relaxation of Fenton-like catalysts, Proc. Natl. Acad. Sci. USA 119 (2022), e2205562119, https://doi.org/10.1073/pnas.2205562119.

[49] Y. Zhao, L. Yu, C. Song, Z. Chen, F. Meng, M. Song, Selective Degradation of Electron-Rich Organic Pollutants Induced by CuO@Biochar: The Key Role of Outer-Sphere Interaction and Singlet Oxygen, Environ. Sci. Technol. 56 (2022) 10710–10720, https://doi.org/10.1021/acs.est.2c01759.

[50] X. Dou, Q. Zhang, S.N.A. Shah, M. Khan, K. Uchiyama, J.-M. Lin, MoS_2-quantum dot triggered reactive oxygen species generation and depletion: responsible for enhanced chemiluminescence, Chem. Sci. 10 (2019) 497–500, https://doi.org/10.1039/C8SC03511C.

[51] N. Du, Y. Liu, Q. Li, W. Miao, D. Wang, S. Mao, Peroxydisulfate activation by atomically-dispersed Fe-N-x on N-doped carbon: Mechanism of singlet oxygen evolution for nonradical degradation of aqueous contaminants, Chem. Eng. J. 413 (2021), 127545, https://doi.org/10.1016/j.cej.2020.127545.

[52] J. He, Y. Wan, W. Zhou, ZIF-8 derived Fe-N coordination moieties anchored carbon nanocubes for efficient peroxymonosulfate activation via non-radical pathways: role of FeNx sites, J. Hazard. Mater. 405 (2021), 124199, https://doi.org/10.1016/j.jhazmat.2020.124199.